

# Anisotropic Dynamics of the JE-2147–HIV Protease Complex: Drug Resistance and Thermodynamic Binding Mode Examined in a 1.09 Å Structure<sup>†,‡</sup>

K. Kinkead Reiling,<sup>§</sup> Nicholas F. Endres,<sup>§</sup> Deborah S. Dauber,<sup>||</sup> Charles S. Craik,<sup>⊥</sup> and Robert M. Stroud<sup>\*,⊥</sup>

*Departments of Biochemistry and Biophysics and of Pharmaceutical Chemistry, Graduate Group in Biophysics, and Graduate Program in Chemistry and Chemical Biology, University of California at San Francisco, San Francisco, California 94143*

Received September 11, 2001; Revised Manuscript Received December 27, 2001

**ABSTRACT:** The structure of HIV protease (HIV Pr) bound to JE-2147 (also named AG1776 or KNI-764) is determined here to 1.09 Å resolution. This highest-resolution structure for HIV Pr allows refinement of anisotropic displacement parameters (ADPs) for all atoms. Clustering based on the directional information in ADPs defines two sets of subdomains such that within each set, subdomains undergo similar anisotropic motion. These sets are (a) the core of monomer A grouped with both substrate-binding flaps and (b) the core of monomer B coupled to both catalytic aspartates (25A/B). The four-stranded β-sheet (1–4 A/B and 95–99 A/B) that forms a significant part of the dimer interface exhibits large anisotropic amplitudes that differ from those of the other sets of subdomains. JE-2147 is shown here to be a picomolar inhibitor ( $K_i = 41 \pm 18 \text{ pM}$ ). The structure is used to interpret the mechanism of association of JE-2147, a second-generation inhibitor for which binding is enthalpically driven, with respect to first-generation inhibitors for which binding is predominantly entropically driven [Velazquez-Campoy, A., et al. (2001) *Arch. Biochem. Biophys.* 390, 169–175]. Relative to the entropically driven inhibitor complexes, the JE-2147–HIV Pr complex exhibits an ~0.5 Å movement of the substrate flaps in toward the substrate, suggesting a more compatible enthalpically driven association. Domains of the protease identified by clustering of ADPs also suggest a model of enthalpy–entropy compensation for all HIV Pr inhibitors in which dynamic coupling of the flaps is offset by an increased level of motion of the β-sheet domain of the dimer interface (1–4 A/B and 95–99 A/B).

Currently, HIV<sup>1</sup> infects 36.1 million individuals worldwide, and is already responsible for a total of 21.8 million deaths (1). Despite recent advances in antiviral agents, the treatment of HIV and AIDS remains one of the most pressing health problems facing both developing and industrialized nations. Drugs have been developed that inhibit two of the three enzymes essential for HIV replication. Nine FDA-approved drugs target reverse transcriptase, while six inhibit HIV protease (HIV Pr). The protease cleaves the viral polyprotein into its separate enzymatic and structural components both in the cytoplasm and in the budded virus to initiate viral particle maturation. Neutralization of the protease through mutation or inhibition results in the budding

of morphologically immature and rapidly cleared viral particles that are no longer infectious (2, 3). Structure-based drug design born of a synergy of medicinal chemistry and X-ray crystallography guided the development of the first-generation drugs that inhibit HIV Pr (4).

Widespread implementation of aggressive drug regimens against reverse transcriptase and HIV Pr has prolonged the lives of millions of infected individuals. Nevertheless, the error-prone nature of the viral polymerase allows rapid adaptation of viral enzymes under the selective pressure of chemotherapeutics. Within the viral population of a single infected individual, each possible point mutation occurs  $10^4$ – $10^5$  times per day for every base of viral DNA (5). Therefore, the viral population within each individual explores sequence space extensively. As a result, the viral population of infected individuals is enriched for and eventually dominated by those viruses expressing altered enzymes that are resistant to antiviral drugs. X-ray crystallography provides both a template and an analytical tool for understanding how drugs can side step drug resistance.

HIV Pr is an enzyme that adapts structurally to recognize and process eight distinct cleavage sites within the viral proteome. Even at resolutions down to 1.45 Å (6) for HIV Pr structures, the data-to-parameter ratio only supports refinement of isotropic “B-factors”, each of which represents a spherical Gaussian approximation of atomic motion. This spherical approximation incorrectly models atomic motion as equal in all directions. The complex of JE-2147, a second-generation inhibitor, with HIV Pr, described here from a

<sup>†</sup> Research supported by NIH Grant GM56531 (R.M.S. and C.S.C.). Graduate fellowship support was provided by NIH Graduate Training Grant GM08204 (K.K.R. and N.E.), an ARCS Foundation grant (K.K.R.), and UARP Grants D99-SF-011 and D00-SF-076 (D.S.D.).

<sup>‡</sup> The coordinates and structure factors have been deposited in the Protein Data Bank entry 1KZK.

<sup>\*</sup> To whom correspondence should be addressed. Telephone: (415) 476-4224. Fax: (415) 476-1902. E-mail: stroud@msg.ucsf.edu.

<sup>§</sup> Graduate Group in Biophysics.

<sup>||</sup> Graduate Program in Chemistry and Chemical Biology.

<sup>⊥</sup> Departments of Biochemistry and Biophysics and of Pharmaceutical Chemistry.

<sup>1</sup> Abbreviations: rmsd, root-mean-square deviation; HIV, human immunodeficiency virus; Pr, protease; AIDS, acquired immunodeficiency syndrome; ADPs, anisotropic displacement parameters;  $K_i$ , inhibition constant; Apns, allophenylnorstatine; Dmt, dimethylthiazolidinecarboxylic acid; NPH, *p*-nitrophenylalanine; ABZ, anthranilyl; COR, center of rotation; TLS, translation, libration, and screw; IC<sub>50</sub>, compound concentration producing 50% inhibition.

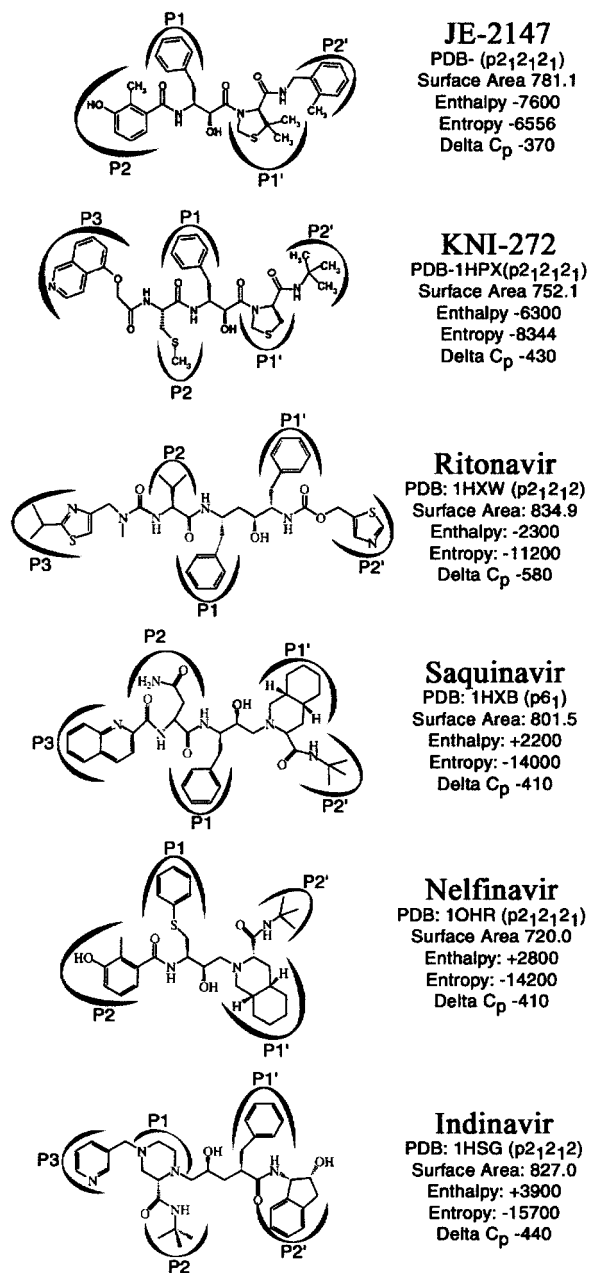


FIGURE 1: Chemical structures of the HIV Pr inhibitors surveyed in this study. The inhibitor structures are represented and labeled from P3 to P2' from left to right. The listed PDB codes and space groups are for the HIV Pr structures used in the structural comparisons. The surface areas buried in respective cocrystal complexes are shown in units of square angstroms. Published thermodynamics data are also shown for JE-2147 (9), KNI-272 (11), and the remainder (12). Entropies and enthalpies were measured at 25 °C. Thermodynamic quantities are listed in calories.

refinement at 1.09 Å resolution, provides the most precise structure of HIV Pr, or of any retroviral protease to date. Data to this resolution allow refinement of anisotropic displacement parameters (ADPs), which provide a basis for interpreting atomic motion in HIV Pr. A dynamic picture of protein mechanics is an important element in the understanding of the mechanisms of drug resistance, and the means of supplanting it.

JE-2147 is an allophenylnorstatine-based transition state analogue (Figure 1) (7) that exhibits a unique resistance profile (8) and thermodynamic binding mode (9). In inhibitor-

resistant strains of HIV Pr, the pattern of mutations can confer cross-resistance to many drugs (reviewed in ref 10). JE-2147, however, is almost as effective against many of these multi-drug-resistant strains as it is against wild-type HIV Pr (8). Rare for HIV Pr inhibitors, JE-2147 ( $K_i = 41 \pm 18$  PM) derives the majority of its binding affinity from enthalpy (9). The properties of JE-2147, including high potency against resistant strains of HIV Pr and its thermodynamic binding mode, are discussed here in the context of the higher dimensionality of the ADP refinement. The JE-2147–HIV Pr complex is compared with other inhibitor–HIV Pr complexes for which thermodynamic data and resistance information are available (11, 12).

## EXPERIMENTAL PROCEDURES

**Determination of  $K_i$  for JE-2147.** Enzyme activity was assayed using the fluorescent substrate ABZ-Thr-Ile-Nle-Leu-NPH-Gln-Arg-NH<sub>2</sub> (13) (Bachem, King of Prussia, PA). All assays were run in the assay buffer [100 mM MES (pH 6.0), 200 mM NaCl, 1 mM EDTA, 20% glycerol, and 0.01% Tween 20]. All rates ( $v$ ) were measured in duplicate at 37 °C in microtiter plates using the ABI SpectraMax Gemini plate reader and SOFTmax software (Molecular Devices, Sunnyvale, CA). The inhibitor concentration ([I]<sub>T</sub>) was varied, and the resulting rates were fit to the Morrison equation (eq 1) (14) to determine the total enzyme concentration ([E]<sub>T</sub>) and  $K_i$ . The reported value represents four separate inhibitor titrations at two different substrate concentrations.

$$\frac{v}{v_0} = 1 - \frac{[I]_T + [E]_T + K_i - \sqrt{([I]_T + [E]_T + K_i)^2 - 4[I]_T[E]_T}}{2[E]_T} \quad (1)$$

**Protein Purification and Crystallization.** HIV Pr used for crystallization was prepared as described previously (15). The protease clone was derived from the drug-naïve, hxb2 HIV-1 strain with the following exceptions: Q7K,<sup>2</sup> which was introduced to prevent autolysis, and K14R, S37N, R41K, L63P, and I64V, which are background polymorphisms. After purification, HIV Pr was concentrated to a final volume of 2 mL using Amicon YM-10 membranes. The protein was concentrated under argon to bring it to a final concentration of ~6 mg/mL. Crystals of HIV Pr were grown by hanging drop vapor diffusion. HIV Pr crystallized in drops composed of a mixture of 2 μL of well buffer and 2 μL of a protease solution. This protease solution contained 20 mM NaAc (pH 5.4), 50 mM NaCl, 1 mM EDTA, 1 mM DTT, and 200 μM JE-2147. Crystallization well buffer contained 1.5 M NaCl, 20 mM NaAc (pH 7.0), 1 mM EDTA, and 1 mM DTT. Platelike crystals grew at 25 °C over the course of 4–5 days; as these crystals began to dissolve, a second rodlike crystal form emerged. This second morphology measured 0.1 mm long by 0.025 mm thick and belonged to space group P2<sub>1</sub>2<sub>1</sub>2<sub>1</sub> with the following unit cell dimensions:  $a = 51.2$  Å,  $b =$

<sup>2</sup> Mutations to the protease are designated with the original amino acid preceding the residue number and the new amino acid following, with both in single-letter amino acid code.

Table 1: X-ray Data Statistics

low-resolution data set	
resolution range (Å)	20–2.35
average $I/\sigma(I)$	34
high-resolution data set	
resolution range (Å)	3.15–1.09
average $I/\sigma(I)$	6.8
no. of observations	433956
no. of unique structure factors	79223
average $I/\sigma(I)$	10.5 (1.1) <sup>a</sup>
space group	$P2_12_1$
unit cell dimensions (Å)	$a = 51.2, b = 58.4, c = 62.9$
$R_{\text{merge}} (\%)^b$	10.4 (75.3) <sup>a</sup>
completeness (%)	99.4 (61.8) <sup>a</sup>
mosaicity (deg)	0.15
Wilson $B$ factor (Å <sup>2</sup> )	6.5
solvent content (%)	34

<sup>a</sup> Values in parentheses represent the highest-resolution bin (1.11–1.09). <sup>b</sup>  $R_{\text{merge}} = \sum|I - \langle I \rangle| / \sum|\langle I \rangle|$ .

58.4 Å, and  $c = 62.9$  Å. The crystals exhibited a solvent content of 34% and harbored a dimer in the asymmetric unit.

**Data Collection and Refinement.** The structure was refined against a 1.09 Å data set collected at SSRL beam line 9-1 using crystals frozen in 20% ethylene glycol as a cryoprotectant. Data were collected in two passes: a high-resolution pass comprising data from 3.15 to 1.09 Å and a low-resolution pass encompassing data from 20.0 to 2.35 Å (Table 1). Diffraction data were integrated, scaled, and merged using the HKL package (16). The structure was determined by molecular replacement methods using either the KNI-272–HIV Pr complex with the inhibitor removed [1hpx (17)] or an apo dimer [3hvp (18)] as a search model (Table 2) in the program AMoRe (19) of the CCP4 suite (20). In both cases, a polyserine model of the dimer was used to minimize sequence bias. Data from 10 to 3.0 Å resolutions yielded a post-rigid body refinement  $R$  value of 37.6% for the closed structure and 47.4% for the open or unliganded structure. The 1hpx-derived polyserine model was then rigid body refined using CNS (21), allowing the monomers to move independently. This model was then refined for 50 cycles using wARP 5.1 (22) with the molecular replacement protocol, against data from 20 to 1.2 Å. Electron density maps showed a shift in the protein backbone for residues<sup>3</sup> 14A–21A and 34A–40A and clearly defined the positions of all atoms of the inhibitor. Manual cycles of model rebuilding were performed using the MOLOC (23) and QUANTA graphical interfaces. Further rebuilding was followed by a second 50-cycle round of wARP refinement, and reduced the  $R$  values to 18.7% ( $R_{\text{free}} = 21.7\%$ ).

All 198 residues of the protease dimer, the inhibitor, and 264 waters were refined by conjugate gradient least-squares

<sup>3</sup> Monomers A and B for the HIV dimer are defined such that when the inhibitor is viewed looking down on the active site of the protease from P2 (left) to P2' (right), monomer A is in the upper position. Positions within the protease are numbered from 1 to 99 with the amino acid type represented using the three-letter codes preceding the residue number and the monomer designation following the number. Waters are numbered such that sequentially numbered waters are spatially clustered, with the exception of the flap water (301), and waters 566, 406, 608, and 426 for ease of comparison to the KNI-272 complex. The published monomer definition for KNI-272 is the opposite of that of other inhibitor complexes. For the purposes of discussion, the monomer definition has been switched to conform to the convention stated above.

Table 2: Refinement Progression ( $R_{\text{work}}/R_{\text{free}}$ )<sup>a,b</sup>

model placement (AMoRe) (20.0–3.0 Å)	37.6%
rigid body refinement (CNS) (20.0–3.0 Å)	36.7%/37.6%
model after refinement “wARP” (20.0–1.1 Å)	18.7%/21.7%
SHELXL97 refinement	
isotropic scaling and $B$ factors (6.0–1.09 Å)	20.08%/23.3% (4σ) & 22.36%/25.36%
ADPs added (6.0–1.09 Å)	14.71%/17.89% (4σ) & 16.50%/20.60%
riding hydrogens added (6.0–1.09 Å)	13.65%/16.54% (4σ) & 15.41%/19.36%
final model ( $W = 0.2$ ) (6.0–1.09 Å)	12.28%/15.50% (4σ) & 14.92%/18.68%
blocked least squares (6.0–1.09 Å)	12.32% (4σ) & 15.20%

<sup>a</sup>  $R_{\text{cryst}} = \sum|F_o| - |F_c| / \sum|F_o|$ . <sup>b</sup>  $R$  values following the ampersand were calculated using all data.

methods against structure factors using SHELX-97 (24). Initial refinement by SHELX-97 exhibited increased  $R$  values (22.4 and 25.4%) without noticeable degradation of the maps. Binning of the  $R$  value by resolution revealed that the bulk solvent correction, as implemented in SHELX-97, poorly modeled the low-resolution data. Therefore, a 6 Å, low-resolution cutoff was instituted for refinement. Multiple conformations for protein side chains were introduced for residues exhibiting alternate conformations in  $1\sigma F_o - F_c$  and  $3\sigma F_o - F_c$  electron density maps. The introduction of ADP tensors for protein and inhibitor atoms further reduced  $R_{\text{work}}$  by 5.8% and  $R_{\text{free}}$  by 4.8% (Table 2) and eliminated difference density around the backbone of many residues. Hydrogens, placed according to stereochemistry, reduced the working and free  $R$  values by an additional 1%. ADPs along bonded directions were restrained to match a standard deviation  $\sigma(\Delta U_{||})$  of 0.01 Å<sup>2</sup> (corresponding to an rmsd of ±0.1 Å). Restraints were also placed on the ADP values of adjacent bonded atoms, perpendicular to chemical bonds ( $U_{\perp}$ ). As refinement converged, these restraints were gradually relaxed until no further improvement in  $R_{\text{free}}$  was observed. The final differences in  $U_{\perp}$  values, between adjacent atoms, were limited to conform, for the protein as a whole, to a normal distribution with a standard deviation  $\sigma(\Delta U_{\perp})$  of 0.4 Å<sup>2</sup> (corresponding to an rmsd of ±0.63 Å). In the final stage of refinement, the structure was subjected to block full-matrix least-squares refinement against all data. Two blocks of roughly 1500 atoms each with a 92-residue overlap between the two (residues 1A–99A with 1B–68B and residues 76A–99A with 1B–99B and all solvent) were alternately and iteratively refined. The final model has 95% of the non-glycine residues in the most favored, eight residues in the additionally allowed, and none in the generously allowed and/or disallowed regions of the Ramachandran plot.

**Structure Analysis.** Protein–inhibitor interactions were annotated utilizing the web-based Ligand-Protein Contacts software (<http://bioinfo.weizmann.ac.il:8500/oca-bin/lpcscs>) (25). Structure alignments were carried out by the method of least-squares superposition as implemented in LSQMAN of the O suite (26). Crystal contacts were annotated using the CCP4 program, CONTACT (27). Multiple interactions of a single residue were tallied as multiple crystal contacts. To describe the rigid body motions of the dimer within the crystal lattice, mean ADPs, the per-residue average over main chain atoms (Cα, C, O, and N), were analyzed. The dependence of the resolved orthogonal components of ADPs with respect to the radius from the center of rotation was

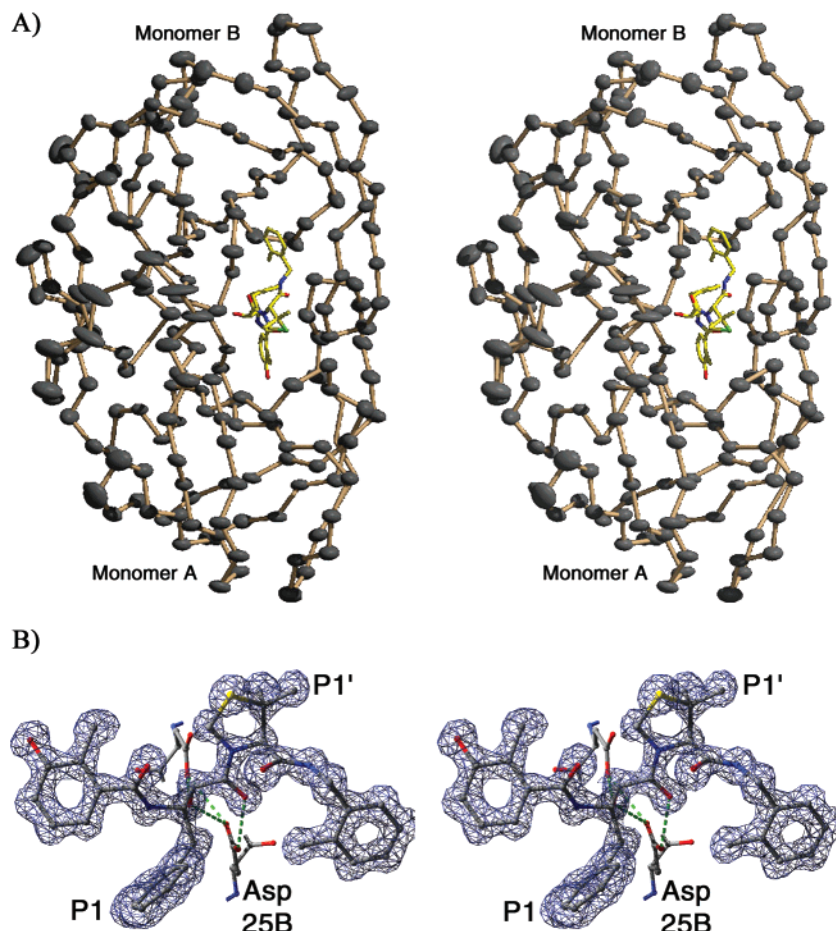


**FIGURE 2:** Representation of the protease dimer and the inhibitor, JE-2147. (A) The  $\text{Ca}$  trace of the protease is shown with the ADP “thermal” ellipsoids represented at the 50% probability level. (B) JE-2147 is shown encased in  $2F_o - F_c$  omit map electron density calculated using the final model refined in SHELXL97 for four rounds with the inhibitor omitted from refinement. The inhibitor is oriented with  $P_2$  to  $P_2'$  from left to right. Active site aspartates (25A/25B) are shown hydrogen bonding to the inhibitor. Panel A was produced with XTALVIEW (48) and panel B with SwissPDBViewer (49) and POVray.

fitted as a linear function of the radius squared using Microsoft Excel. Translation, libration, and screw (TLS) tensors describing rigid body motions were fitted to the atomic ADP tensors using the CCP4 program ANISOANAL (28). Analysis of TLS tensors was performed with the program TLSANL (29), also in the CCP4 package.

The  $\Delta$  matrix, used for clustering, was generated using ANISOANAL. CLUSTER (30), a program developed for the analysis of gene expression data, was used to assemble residue blocks of this  $\Delta$  matrix with similar ADP amplitudes and direction profiles. No manipulation or filtering of the  $\Delta$  matrix was carried out within the CLUSTER program. The rows of the  $\Delta$  matrix were compared using a centered correlation coefficient, which does not assume that the averages of the profiles being compared are similar. Clustering of residue blocks with each other and existing nodes was done using an average linkage metric. This metric uses the average of all members of a node as the standard against which new candidate blocks are compared. Averaging the ADP profiles over a node should accentuate the common motions of that node. As a test of this clustering method, a Spearman rank-order clustering was also performed, again using average linkage between nodes. Spearman clustering produced a tree similar to the centered correlation coefficient treatment. A background for the clustering was established by randomly and extensively permuting the elements of the

$\Delta$  matrix and then clustering in an identical manner. The highest correlation exhibited by the randomized  $\Delta$  matrix (0.7) was used as a guideline when evaluating the clustering of the native ADP profiles. The resultant trees and clusters were visualized using the program TREEVIEW (30).

## RESULTS

The crystal structure of the JE-2147–HIV Pr complex positions all 198 amino acids of the protease dimer (Figure 2A). Eleven residues in the dimer exhibit multiple side chain conformations: Gln2A, Thr4A, Lys43A, Thr91A, Cys95A, Glu21B, Met46B, Cys67B, Lys70B, Val82B, Leu97B, and Asn98B. The dimer has an average isotropic  $B$  factor for all atoms of  $12.9 \text{ \AA}^2$  and an average anisotropy, the ratio of the ADP ellipsoid’s shortest principal axis to the longest (each proportional to the square of the amplitude of displacement), of 0.38 as compared with an average value of 0.45 found in other structures refined at a comparable resolution (Table 3) (31). The structure of the JE-2147–HIV Pr complex exhibits no gross conformational difference when compared with other inhibitor–HIV Pr cocrystal structures ( $\text{Ca}$  rmsd of  $0.6 \text{ \AA}$  vs structures listed in Figure 1).

**JE-2147 Binding.** JE-2147 is a tetrapeptide mimetic built on a  $P_1$  allophenylnorstatine (Apns)– $P_1'$  dimethylthiazolidinecarboxylic acid (Dmt) backbone.  $P_2$  (3-hydroxy-2-methylbenzoylamine) and  $P_2'$  (2-methylbenzylcarboxamide)

Table 3: Refinement Parameters and Statistics of the Final Structure

no. of residues	198
no. of non-hydrogen atoms	
protein	1554
inhibitor	41
water	223
other solvent	24
no. of observations/no. of parameters	73360/16580
deviation from ideality (rmsd)	
bond distances (Å)	0.016
angles (deg)	0.035
coordinate errors from least-squares inversion [average (Å) <sup>a</sup> ]	
protein atoms (main chain)	0.024 ( $\sigma = 0.006$ )
protein atoms (side chain)	0.025 ( $\sigma = 0.015$ )
inhibitor	0.024
water	0.069 ( $\sigma = 0.049$ )
Cl ion	0.013 ( $\sigma = 0.030$ )
ethylene glycol	0.063 ( $\sigma = 0.019$ )
Equivalent Isotropic <i>B</i> and Anisotropy [Mean ( $\sigma$ )]	
	<i>B</i> (Å <sup>2</sup> )
	anisotropy
main chain atoms	10.3 ( $\sigma = 3.4$ )
side chain atoms	15.6 ( $\sigma = 9.7$ )
inhibitor atoms	8.7 ( $\sigma = 1.4$ )
water atoms	25.3 ( $\sigma = 12.1$ )

<sup>a</sup> The coordinate error for each group is the average of the error for each atom. Listed with each group average is the standard deviation about the average.

are modified phenolic rings with different linker lengths. The inhibitor binds in one unique orientation with unambiguous  $2F_o - F_c$  “omit map” density for the entire molecule (Figure 2B). JE-2147 buries a total solvent accessible surface area of 781 Å<sup>2</sup> out of a possible 806 Å<sup>2</sup> (96% of the total surface for the inhibitor alone) in the complex. This is comparable to an average total burial of 787 Å<sup>2</sup> out of a possible 894 Å<sup>2</sup> (88% of the total surface) for the other inhibitors for which there is thermodynamic data (Figure 1). Hydrophobic to hydrophobic contacts comprise 592 Å<sup>2</sup> of the surface of interaction of JE-2147 with HIV Pr. The asymmetry of the inhibitor induces asymmetry in the C2 symmetric HIV Pr dimer with an rmsd between the two monomers of 0.61 Å for Cα atoms and 1.08 Å for all atoms.

**P3 and P2 Water Cage.** JE-2147 is a compact and highly potent inhibitor, with an inhibition constant ( $K_i$ ) of  $41 \pm 18$  pM against wild-type HIV Pr. Although JE-2147 lacks the P3 substituent found in the parent compound, KNI-272, the two inhibitors have comparable potencies (IC<sub>50</sub>s of 30 and 27 nM, respectively) in a cell-based assay (8). The retention of potency by JE-2147, despite its reduced molecular mass relative to that of KNI-272, may be linked to the higher proportion of JE-2147 that becomes solvent inaccessible upon binding: 96% versus 86% for KNI-272 (buried surface/total surface of inhibitor) (17). Removal of the P3 substituent allows tighter packing of Arg8B into the P1–P2 bridging region, and tighter packing of Pro79B against the P1 phenyl group of JE-2147. The guanidinium group of Arg8B is then able to participate in a water cage (waters 95, 96, 97, and 197), coordinated by residues Asp29A, Asp30A, Arg8B, and Gly48B, which shields the hydrophobic P2 and P1 substituents of JE-2147 from the bulk solvent (Figure 3A). The reduced length of JE-2147, as compared with KNI-272, constricts the substrate exit portals of the dimer, thereby shielding the inhibitor from solvent and minimizing entropic costs of ordering surface water molecules.

**S2 and S2' Binding Pockets.** Small structural differences between the P2 and P2' positions of JE-2147 produce different packing of the inhibitor in the S2 and S2' binding pockets. The P2 and P2' moieties of JE-2147 are phenyl rings with differential modification: the P2 ring has ortho and meta substitutions, while the P2' ring contains only an ortho substituent. The P2 *m*-hydroxyl forms a hydrogen bond with O $\delta_2$  of Asp30 [Figure 3A,C ( $2.68 \pm 0.03 \text{ \AA}$ )]. The P2 *O*-methyl group points into the S2 pocket burying  $51.8 \text{ \AA}^2$  (29% of the total for P2). In a related inhibitor, the addition of two groups equivalent to these improves the percentage of enzyme inhibition observed at a compound concentration of  $5 \mu\text{M}$  from 52 to 97% (7). The P2' *O*-methyl packs more deeply into the S2' pocket than does the P2 *O*-methyl into the S2 pocket. As compared to the P2 ring, the P2' ring rotates roughly  $60^\circ$  toward the interior of its pocket, resulting in a closer approach of the P2' *O*-methyl to Ile84B C $\delta_1$  (4.10 vs  $4.32 \text{ \AA}$  for Ile84A and the P2 *O*-methyl) and altering the conformation of Val32B ( $180^\circ$  about  $\chi_1$  relative to Val32A). Addition of a homologous P2' *O*-methyl in a related inhibitor improves the  $K_i$  6-fold (7). The flaps interact with one face of each of the P2' and P2 rings. The side chains of Ile50A and Ile47B distribute interactions across the P2' ring. Packed less deeply, the P2 ring is less well positioned to make similar van der Waals interactions with Ile50B and Ile47A. As a result of this asymmetry, the S2' flap of monomer A (49A and 50A) is shifted  $\sim 0.5 \text{ \AA}$  toward the active site when compared with the S2 flap (49B and 50B) (Figure 4A).

**S1 and S1' Binding Pockets.** Asymmetry in the P1 and P1' positions of the inhibitor induces asymmetry in the S1 and S1' pockets. Substituents of the P1' position affect the water structure in the S1' pocket. The smaller size of the P1' position of the inhibitor, as compared to P1, results in a tighter association of the 80s loop of monomer A with P1' than of the 80s loop of monomer B with P1 (Figure 4A). The two methyl substituents of the P1' Dmt ring make the primary contacts with the S1' pocket, burying 97 Å<sup>2</sup> of the solvent accessible surface (59% of the total for P1'). The P1' Dmt ring is puckered compared to the P1' ring of KNI-272, which shifts the backbone of the inhibitor by 0.8 Å and positions a methyl deep within the S1' pocket (Figure 3B). Water607, seen in crystallographic and NMR studies of KNI-272 (17, 32), is displaced by this P1' methyl. The contacts made and the water liberated by the methyl groups contribute to the 27-fold enhancement in  $K_i$  upon addition of the methyl groups (7). The addition of P1' methyl groups to either KNI-272 or JE-533 (JE-2147 with a KNI-272 like P2' *tert*-butyl) improved binding 8.4- or 4.8-fold, respectively (7, 33). These improved affinities demonstrate that the P1' methyl groups and the subsequent displacement of water607 are advantageous for inhibitors containing an Apns-thioproline P1-P1' backbone.

*Hydrogen Bonding and the Inhibitor.* JE-2147 participates in five inhibitor–protein and three water-mediated hydrogen bonds, with the majority of this enthalpic potential located at the active site (Figure 3B,C). The water-mediated bonds include the canonical HIV Pr water bridge (water301), which connects the P2 and P1' backbone carbonyls to the flaps, and a water bridge (water608) from the backbone amide of Asp29B to the P2' amide. Replacement of this P2' amide with an ester linkage reduces binding affinity by 1 order of magnitude in a related inhibitor (34), implicating it in

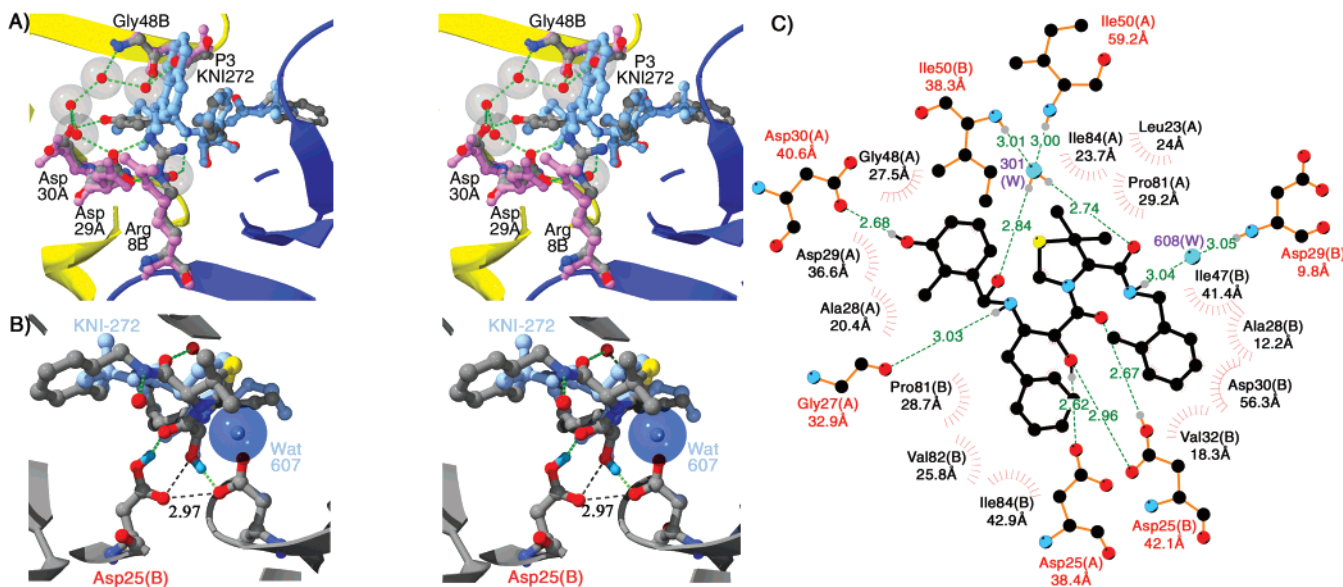


**FIGURE 3:** Interaction of JE-2147 with the protease. (A) The lack of a P3 moiety in JE-2147 allows movement of Arg8B toward the P2 residue, as compared to the KNI-272 structure. Arg8B of the JE-2147–HIV Pr complex is seen to participate in a water cage not seen associated with KNI-272 and which shields JE-2147 from solvent. The JE-2147 P2 water cage waters are represented with hard-sphere atom centers and semitransparent van der Waals surfaces. The coloring is as follows: the KNI-272 compound, light blue; protease residues from the the KNI-272–HIV Pr structure, light purple; JE-2147 compound and protease residues, CPK; ribbons from the JE-2147–HIV Pr complex, yellow for monomer A and blue for monomer B. (B) A stereorepresentation of the active site hydrogen bonds in the JE-2147–HIV Pr complex is provided. Overlaid upon JE-2147 is KNI-272 (light blue) illustrating the increased pucker in the thioproline ring of JE-2147 and the shift in the JE-2147 backbone. Water607 of the KNI-272 structure is shown with a semitransparent van der Waals surface. Notice that the P1' methyls of JE-2147 will not sterically allow this water. (C) The major interactions of JE-2147 with HIV Pr are depicted schematically here along with hydrogen bond lengths and deduced positions of hydrogen atoms. Also listed is the buried surface area for each residue. The representation is as a LIGPLOT figure (50).

inhibitor positioning (17). The active site aspartates make three hydrogen bonds to the carbonyl and hydroxyl groups of the P1 backbone. NMR studies (32) and computer simulations (17) of KNI-272 indicate that, in the context of an Apns-based inhibitor such as JE-2147, Asp25B is protonated while Asp25A is not. In our structure, O $\delta_2$  of Asp25B is involved in a short hydrogen bond ( $2.67 \pm 0.03$  Å) to the P1 carbonyl of JE-2147, which is consistent with the protonation of O $\delta_2$ . The P1 hydroxyl participates in a short hydrogen bond with Asp25A O $\delta_1$  ( $2.62 \pm 0.03$  Å). The carboxyl groups of the two aspartates are not coplanar with their C $\gamma$ , O $\delta_1$ , and O $\delta_2$  atoms deviating 0.23 Å from the least-squares plane through the two carboxyl groups. The short hydrogen bonds between Asp25B O $\delta_1$  and Asp25A O $\delta_2$  and the inhibitor P1 hydroxyl and carbonyl are candidates for enthalpic binding determinants of JE-2147.

**ADPs: Temperature Factors and Anisotropy.** Anisotropic ADPs (related to  $B$  factors by the relation  $U = B/8\pi^2$ ) can highlight concerted or correlated atomic motions of non-bonded groups influenced by, for instance, enthalpy-driven associations. As an example, the four-stranded  $\beta$ -sheet that crosses the dimer interface has isotropic  $B$  factors that are higher than the average for the rest of the protein (Figure 5A,B). The displacements in this region are anisotropic and predominantly in the plane of the  $\beta$ -sheet, indicating a correlated motion of the sheet as a whole (Figure 6A). The amplitudes of displacement are larger in the half of the  $\beta$ -sheet that contains the N-terminal strand of monomer A and the C-terminal strand of monomer B. This half of the  $\beta$ -sheet exhibits a larger average  $B$  factor ( $15.5 \text{ \AA}^2$ ) and a greater degree of anisotropy (0.28) than that of the other half of the dimer interface ( $14.8 \text{ \AA}^2$  and 0.35, respectively). The

$2F_o - F_c$  density for Thr4A shows two distinct substates for both main chain and side chain atoms (Figure 6B), consistent with NMR evidence discussed later. The mean and standard deviation of the isotropic  $B$  factors demonstrate that this four-stranded  $\beta$ -sheet has higher  $B$  factors in the JE-2147–HIV Pr complex than in other HIV–inhibitor structures (Figure 5B). Both monomers of the structures that have been surveyed (PDB entries listed in Figure 1) and monomer B of the JE-2147–HIV Pr complex all participate in a crystal contact at Trp6, which might dampen motion within the four-stranded  $\beta$ -sheet. The lack of a contact at Trp6A in the JE-2147–HIV Pr complex suggests that the heightened temperature factors and anisotropy of the more mobile side of the  $\beta$ -sheet may better reflect the natural mobility of this region in solution for the JE-2147–HIV Pr complex.

*ADPs: Separating Lattice Disorder (Rigid Body Motion) from Atomic Motion within the Molecule.* To evaluate anisotropic motion of individual atoms with respect to the protein molecule as a whole, it is necessary to estimate the component of atomic ADPs that could arise from global, possibly anisotropic, disorder within the lattice. In addition to crystal lattice disorder, “frozen” rigid motions of the enzyme contribute to this global background anisotropy. Rotational background anisotropy of the dimer as a rigid body contributes to individual atomic ADPs ( $\mu$ ) as a product of the radius ( $r$ ) from some apparent center of rotation (COR) and the angular magnitude ( $\omega$ ) of the “rotation” ( $\mu = wr$ ). ADPs are proportional to the square of the average atomic displacement of an atom ( $U_{ij} = \langle \mu_i \mu_j \rangle^2$ ) from its refined position. Therefore, the component of each ADP tensor due to rotational background anisotropy will appear as a linear

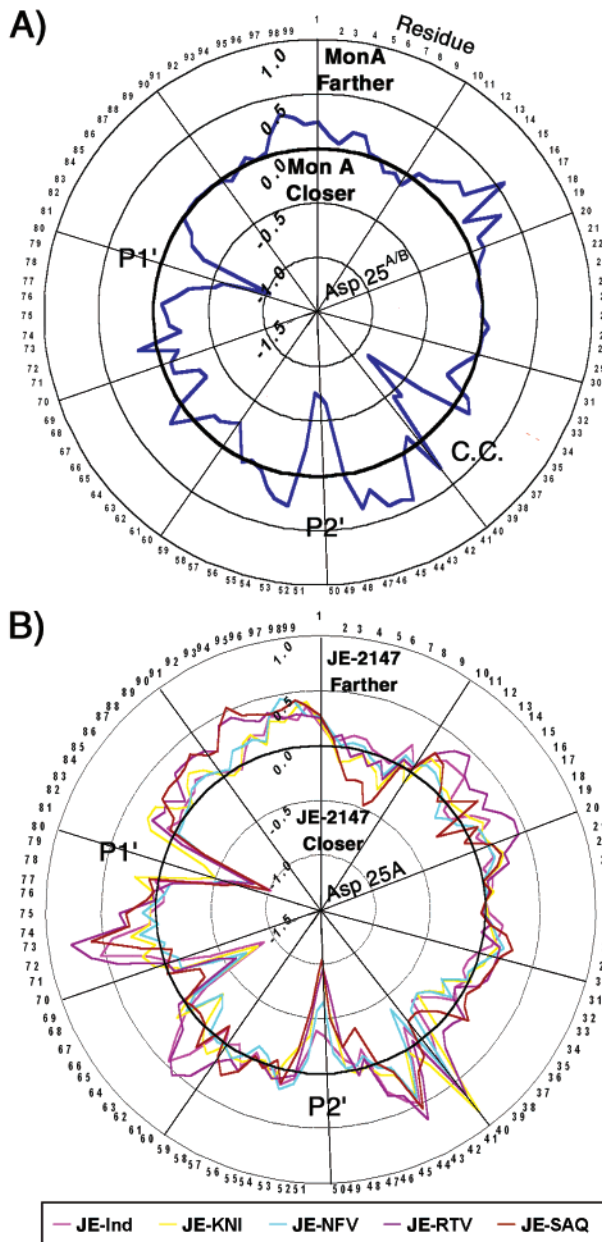


FIGURE 4: Structural comparison of active site loop interactions of HIV Pr. The “clamping down” by the flaps of monomer A is visualized by taking the difference distance for the C $\alpha$  atom of each residue with respect to the C $\alpha$  atom of the active site aspartates of the same monomer. The double difference values are plotted radially with values toward the center indicating a closer approach to the active site aspartates. (A) Radial plot for monomer A vs monomer B of the JE-2147–HIV Pr complex. (B) Radial plot for monomer A of the JE-2147–HIV Pr complex compared to monomer A of the HIV Pr structures listed in Figure 1. Note the compression of the flaps and the 80s loop in monomer A denoted in the figure by P2' and P1', respectively. The JE-2147–HIV Pr complex is compared to that of HIV Pr complexed with KNI-272 (yellow), with ritonavir (purple), with nelfinavir (pink), and with saquinavir (brown).

functional dependence on the square of the distance from the COR ( $B_{\text{rigid}} = 8\pi^2 U = 8\pi^2(\omega r)^2$ ).

The ADPs of the backbone of the protease were analyzed to detect rotational background anisotropy. The projection of each residue's average ADP tensor onto and perpendicular to its radial vector from the COR of the dimer was calculated ( $U_{\text{radial}}$  and  $U_{\text{tangential}}$ , respectively). Both projections were

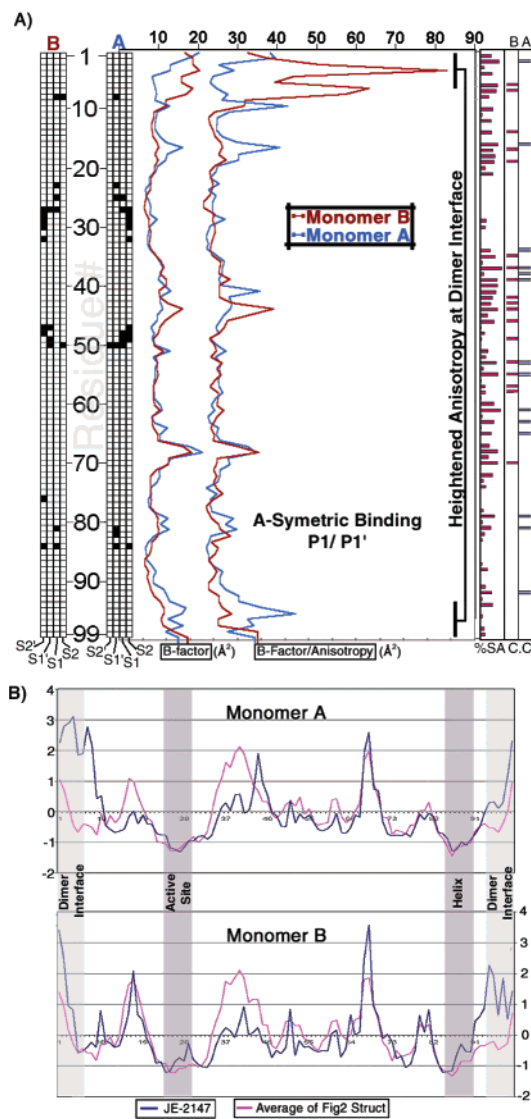


FIGURE 5:  $B$  factor analysis of the JE-2147–HIV Pr complex. (A) The central chart plots the average isotropic  $B$  factors for the main chain atoms of both monomer A (blue) and monomer B (red). The traces on the right side of the graph are the ratios of the average isotropic  $B$  to the average anisotropy of the main chain atoms for each monomer. This ratio provides profile information for the directional character of anisotropic thermal parameters with higher numbers indicating greater deviations from a spherical character. The first column to the right of the temperature factor plot is a histogram of the percent solvent accessibility of each residue, allowing the evaluation of the effects of exposure on mobility. For clarity, the average of the two monomers is displayed. The two columns on the far right are binary indicators of the presence of crystal contact at each residue: bars on the left are for monomer B and the bars on the right are for monomer A. For the two columns to the left of the  $B$  factor chart, a darkened square indicates that a residue comes in contact with the inhibitor. The left column is for monomer B and the right column for monomer A. (B) The  $B$  factors of the surveyed structure were normalized to allow direct comparison of their per-residue thermal factors. Each of the surveyed structures was normalized by subtracting the average isotropic  $B$  factor of the structure as a whole from the average backbone isotropic  $B$  factor of each residue. These “corrected”  $B$  factors were then divided by the variance of the structure to obtain the  $\sigma$  from the mean  $B$  factor for each residue. The average of the other surveyed structures is shown for clarity beside that for the JE-2147–HIV Pr complex. Note the heightened temperature factors of the dimer interface  $\beta$ -sheet of the JE-2147–HIV Pr complex and the uniform correlation between the active site and the helices in all the HIV Pr structures that have been surveyed.

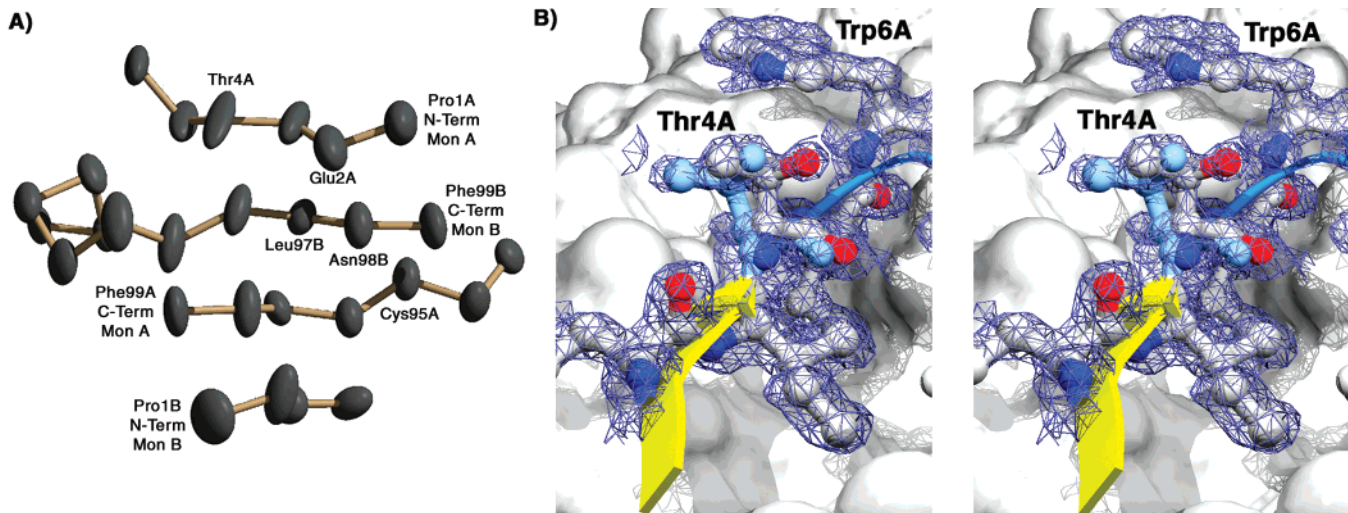


FIGURE 6: Disorder in the four-stranded  $\beta$ -sheet that crosses the interface of the JE-2147–HIV Pr complex. (A) Pictured is the  $C\alpha$  trace of the dimer interface with each atom scaled to a 50% probability sphere for its ADPs. Labeled are the N- and C-termini of each monomer and the residues in the dimer interface exhibiting multiple side chain conformations. (B) Pictured is the bifurcated density for residue Thr4A, which is an extreme but telling example of the conformational flexibility of the interface. Panel A was produced with XTALVIEW (48) and panel B with SwissPDBViewer (49) and POVray.

Table 4: Upper Limits for the Contribution of Rigid Body Motions and Lattice Disorder to ADPs<sup>a</sup>

	libration ( $\text{deg}/\text{\AA}^2/\%\text{/}\text{\AA}^2$ )	translation ( $\text{\AA}/\text{\AA}^2/\%\text{/}\text{\AA}^2$ )
monomer A	0.838/3.2/26/12.5	0.092/7.2/58/12.5
monomer B	0.839/2.9/22/13.2	0.097/7.2/55/13.2
dimer	0.771/2.7/21/12.9	0.099/7.8/60/12.9

<sup>a</sup> Included for each rigid body are, from left to right, the mean deviation (libration in degrees and translations in angstroms), the average  $B$  factor as a result of the application of the libration or translation, the percentage of the final refined  $B$  factor this rigid body temperature factor represents, and the final refined average isotropic  $B$  for each domain.

graphed as a function of the radius squared ( $r^2$ ).  $U_{\text{tangential}}$  was fitted to a straight line with slope of 0.0067 and an intercept of  $9.05 \text{ \AA}^2$ . This linear fit exhibited an  $R^2$  value of 0.43, which indicates that rigid body librational motions of the dimer account for roughly 40% of the observed variance in atomic anisotropy. As expected, the fit of  $U_{\text{radial}}$  to  $r^2$  indicates no radial dependence: slope of 0.0005, intercept of  $7.77 \text{ \AA}^2$ , and  $R^2$  of 0.006.

To ascertain the character of the global background anisotropy, the ADPs of the dimer or of each monomer of the protease were fitted to rigid body translation, libration, and screw tensors (TLS). TLS refinement seeks a least-squares fit of each defined region's ADPs to rigid body motions of that region. The magnitudes of the TLS tensors, therefore, serve as an upper limit for rigid body contributions to atomic motion (Table 4). In addition, TLS refinement determines the point at which libration and translation of a rigid body are decoupled, or the center of rotation (COR). When fitted either as a dimer or as separate monomers, the COR lies within monomer B. This COR position is consistent with the larger number of stabilizing crystal contacts made by monomer B (40 vs 28 for monomer A) and indicates that the predominant motion of the monomers is communal. The radial dependence and rigid body fitting of the ADPs imply that global background anisotropy can account for between 40 and 80% of the anisotropy of the dimer. The remainder of the individual ADPs is due to local atomic fluctuations.

**ADPs: The Rigid Body Postulate.** Overlaid on the global background anisotropy of the dimer are rigid or quasi-rigid motions of substructures of the protease. ADPs can be used to identify regions of the protein separated in primary sequence whose displacement parameters are similar and so may have correlated motions. The “rigid body criterion” (35) states that the difference between the projections of ADPs of two groups onto a vector connecting them will approach zero if they are moving as a rigid body. We calculated these differences for the JE-2147–HIV Pr complex and arrayed them into a  $\Delta$  matrix, the elements of which are the ADP differences between main chain atoms of each two-consecutive-residue block of the HIV Pr dimer with each other two-consecutive-residue block; i.e., row 1 contains differences for residues 1A and 2A with 1A and 2A, 3A and 4A, and 5A and 6A, to 98B and 99B. The rows of the  $\Delta$  matrix provide an ADP–tensor correlation profile for each two-residue block of the protein. While the absolute values of individual elements of this array may fluctuate very little, we effectively increase the signal-to-noise ratio by comparing the profiles of the residue blocks. Profiles that are highly correlated suggest regions of the protease that are affected by similar rigid body motions relative to the rest of the protein. The rows of this  $\Delta$  matrix were clustered, and the nodes of the resulting tree were mapped to the JE-2147–HIV Pr complex using a correlation coefficient of 0.7 as a relevance guideline (see Experimental Procedures). The closest clustering of two residues involved in a crystal contact occurs between residues 43B and 61A, which are in distal sections of cluster 1. This weak relation indicates that there are minimal clustering biases due to the crystal contacts. The motions of the protease subdomains, suggested by the clustering, were then modeled by fitting the displacement parameters of each group to rigid body motions as described by TLS tensors.

The ADP profile clustering identified two large clusters that each traverse the dimer, and two loose collections of surface residues (each cluster is defined in Figure 7). Cluster 1 consists of residues from the core  $\beta$ -sheet of monomer A

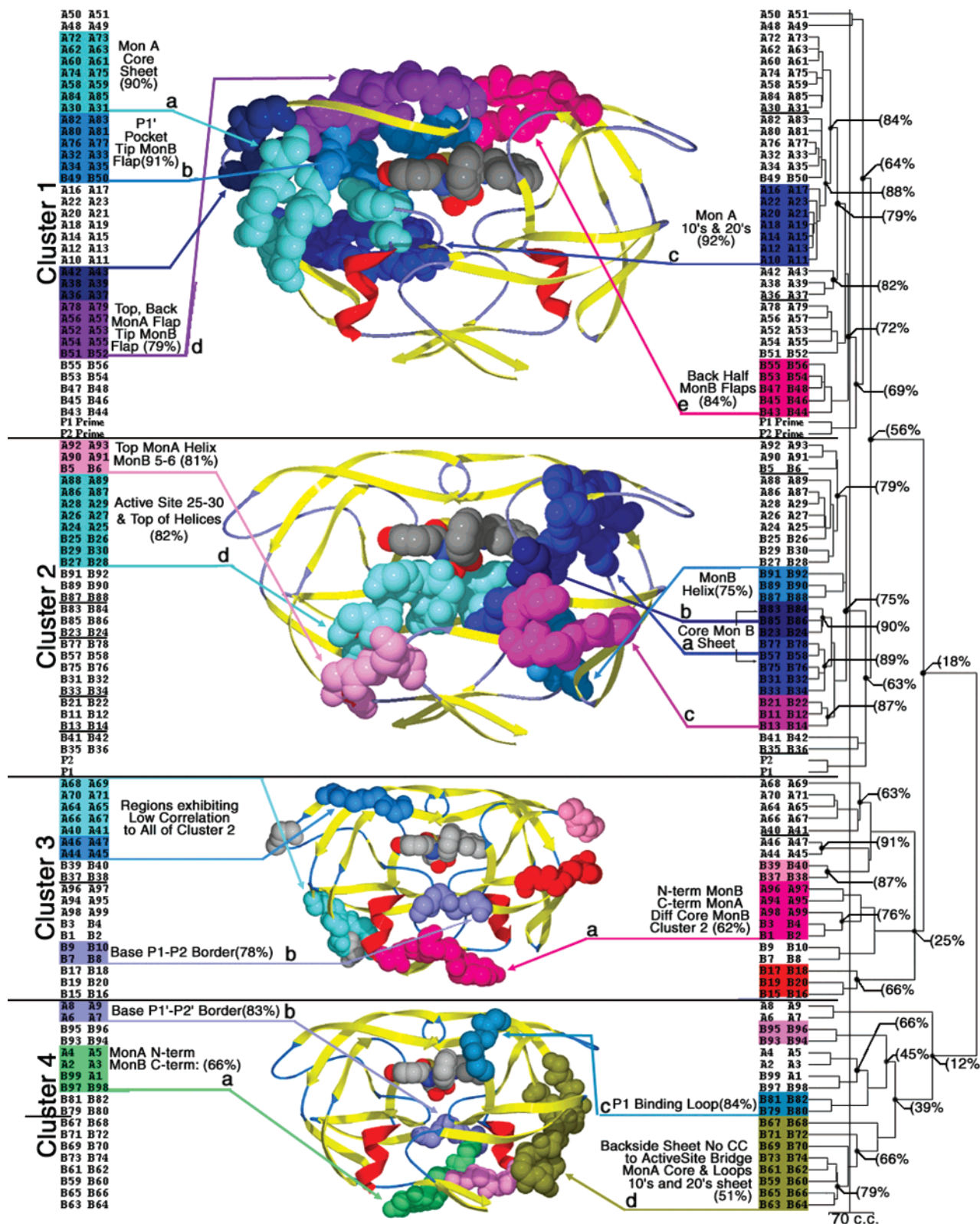


FIGURE 7: ADP profile clusters of the JE-2147–HIV Pr complex. The same color scheme used in the central structures is repeated in the cluster trees on either side. The two residue listings are identical and included for increased clarity. Subclusters discussed in text are labeled at the end of each cluster bar. The nodes are marked with the correlation coefficient associated with that branch point. The labeled subdomains have included in their labels a percentage that indicates the correlation coefficient linkage for that cluster. Images were produced with SwissPDBViewer (49) and POVray.

(residues 30, 31, 58–63, 72–75, 84, and 85 in monomer A), and the S1' and S2' binding pockets and the flaps of both monomers (residues 32A–35A, 51A–57A, 76A–83A, 43B–50B, and 53B–56B). Not surprisingly, the ADPs of

the prime side of the inhibitor cluster to this region of the protease (correlation coefficient of 0.7). TLS tensor analysis indicates that the predominant rigid body motions of the tip of the flaps of monomer B (49B and 50B), and the S1'

pocket, are directed into and out of the active site cleft. This implied motion is suggestive of a degree of freedom required for opening and closing of the active site of the protease. Cluster 1 appears to coalesce via interactions among monomer A's substrate loops and monomer B's flap, which are in turn associated with the core of monomer A.

Cluster 2 contains the active sites of the two monomers and the core  $\beta$ -sheet of monomer B. The active site of the protease, composed of residues 24–30 from each monomer, bridges between monomers and exhibits concerted motion, in the plane of the inhibitor backbone (Figure 7, cluster 2d). TLS analysis of cluster 2, as a whole, indicates that its communal motion is essentially the same as that of the active site when fitted alone, with rotation axes centered on the catalytic aspartates. This harmonic or anharmonic fluctuation of the active site catalytic residues and the residues that anchor them in the binding site may relate to proton shuttling between the catalytic aspartates (36).

Clusters 3 and 4 are distantly related to clusters 1 and 2 by a correlation of only 18%. Cluster 3 includes the N-terminus of monomer B and the C-terminus of monomer A. These two strands, when fitted to TLS tensors, together exhibit rotations in the plane of the  $\beta$ -sheet along a vector parallel to and between the two strands. Cluster 4 includes the other half of the four-stranded, interface  $\beta$ -sheet, which exhibits large translations in the plane of the interface (Figure 6A). These two loose clusters each contain one of the P1–P2/P1'–P2' border pockets (6A/B–10A/B). These border regions exhibit librations into and/or out of the binding pockets as seen above for the P1–P1' binding loops (cluster 1b, 4c).

Clustering of the JE-2147–HIV Pr complex subdivides the enzyme into a region comprising the P1' pocket, the P2' pocket, and the core of monomer A and a separate region to include the active site and the core of monomer B. The dimer interface of the protease clusters separately from the core of the monomers, indicating an independent direction and amplitude of motion. Thus, to the extent that ADP profiles depend on nonbonded interactions (within clusters) and indicate the independence of protease domains (between clusters), ADP analysis highlights strong interactions among the binding loops of HIV Pr and dynamics of its dimer interface upon binding of JE-2147.

## DISCUSSION

Although HIV Pr inhibitors interact with the same general binding site on the enzyme, they have different thermodynamic binding end points and different resistance susceptibilities. The high resolution of the current structure allows the refinement of HIV Pr incorporating ADP tensors, and so allows the subsequent evaluation of drug binding and drug resistance in the context of a more dynamic representation of the HIV Pr structure.

**Resistance.** JE-2147 has a resistance profile distinct from that of other inhibitors, inhibiting several strains of multi-drug-resistant proteases with a lower impact factor (ratio of  $K_i$  values) due to resistance mutations in the protease (8). This is not to say that JE-2147 is unencumbered by resistance. The mutations L10F, M46I, I47V, and I84V arise in cell culture in the presence of JE-2147, and reduce the binding affinity of JE-2147 for HIV Pr (28-fold increase in

$IC_{50}$ ) (8). Although the mutations raised against JE-2147 occur individually in response to other drugs, the particular pattern of mutations is unique to JE-2147; It is a pattern not found in the Stanford Protease Sequence Database [<http://hivdb.stanford.edu/PRMut.pl>] (37)].

Of the JE-2147 resistance mutations, I47V appears to have the greatest contribution to the reduction in the level of binding. Residue Ile47B interacts primarily with the P2' position of JE-2147, burying 47.1  $\text{\AA}^2$  (all cited areas refer to solvent accessible surface areas of the inhibitor that are buried upon complexation). The related inhibitor, JE-533, which differs from JE-2147 only by the substitution of a *tert*-butyl group for the aromatic ring in the P2' position, is 10-fold more effective against the I47V strain than is JE-2147. In the structures of KNI-272 and nelfinavir bound to HIV Pr, an analogous *tert*-butyl group at P2' does not extend into the S2' pocket as far as the P2' ring of JE-2147, thus interacting less extensively with Ile47B (20 and 26  $\text{\AA}^2$  for KNI-272 and nelfinavir, respectively). The I47V mutation would affect, to a lesser degree, the S2 pocket where Ile47A shares 20.9  $\text{\AA}^2$  of contact area with JE-2147. The hydrogen bond from Asp30 to the P2 hydroxyl and the identical P2 moieties in JE-2147 and JE-533 suggest that resistance due to I47V is mediated more at the S2' site. The I84V mutation develops in response to JE-2147, JE-533, and KNI-272 and may represent an Apns class resistance mutation. This mutation would trim the hydrophobic surface area of the protein available for inhibitor binding at the S2–S1' and S1–S2' borders by 24 and 40.5  $\text{\AA}^2$ , respectively. Thus, I47V appears to be a primary JE-2147 resistance mutation, and I84V may act against all Apns inhibitors.

**Closing of the Flaps around JE-2147.** Accompanying the clustering of the flaps of monomer A based on their ADP profiles is a particularly tight conformation of the flaps against the P1' and P2' positions of JE-2147. When compared to other inhibitor complexes, the primary binding flap of monomer A (49A–52A) is 0.2–1.2  $\text{\AA}$  ( $\sim 1.5\sigma$ ) closer to the active site (Figure 4B). Although this region of the protease is involved in a crystal contact, this crystal contact is common to all the examined structures. The intimate packing of the monomer A flap is accompanied by a more planar arrangement of the side chain of Ile50A, a structural feature unique to the JE-2147–HIV Pr complex. In other complexes, a closer approach of the flaps is sterically hindered by nonplanar groups at P2', such as the *tert*-butyl present in KNI-272. In the S1' pocket, the 80s loop of monomer A packs closer to the active site than is seen in the inhibitor complexes indicated in Figure 1.

Previous molecular dynamics studies on the flaps and chimeric constructs of the flaps characterize them as crucial determinants of substrate binding and resistance (38–40). In the case of macrocyclic peptidomimetics, tighter packing of the active site loops of HIV Pr has been correlated with increased binding affinity (41). Clustering of the protein on the basis of ADP interaction profiles indicates that the flaps of monomer A and B and the P1' binding loop exhibit similar anisotropic motions possibly due to interactions among the flaps. The closer, more extensive packing of the active site loops to JE-2147 may optimize van der Waals interactions both between the inhibitor and the active site and within the active site itself. In this manner, the packing of the flaps

may contribute to the more favorable enthalpy of binding of JE-2147 relative to other inhibitors.

**Thermodynamics of Inhibitor Binding.** JE-2147 binding is enthalpically driven, in contrast to that of the entropically dominated first-generation HIV Pr inhibitors (9). When the enthalpy and entropy values for the first-generation inhibitors are linearly extrapolated to a physiological temperature (37 °C) (9, 11, 12) from 25 °C, at which they are reported, all inhibitors are in fact enthalpically favorable. This extrapolation was performed assuming no temperature dependence for the reported heat capacities (listed in Figure 1). JE-2147 and KNI-272 derive the majority of their binding affinity from enthalpy (64 and 57%, respectively, vs an average of 17% for the first-generation inhibitors). For KNI-272, six long-lived water molecules, seen in both the crystal and NMR structures of the complex, were hypothesized to provide a hydrophilic and thus enthalpically favorable mask for the inhibitor (11). All of these waters, with the exception of the displaced P1' water (wat607) discussed earlier, are present in the JE-2147–HIV Pr complex and in at least one of the crystal structures from the entropically driven class of inhibitors. Displacement of the P1' water in our structure, without concomitant loss of binding enthalpy, suggests that this water is not central to the enthalpic interactions of this inhibitor. Finally, JE-2147 exhibits a more favorable binding enthalpy than KNI-272, suggesting that the enthalpy of binding in the Apns class of inhibitors is due to more subtle determinants than previously thought.

JE-2147 presents two hydrogen-bonding moieties to the active site aspartates of HIV Pr. The P1 hydroxyl of the Apns inhibitor class is known to contribute to binding enthalpy, because substitution of the opposite stereoisomer in KNI-272 reduces the binding enthalpy by 2 kcal/mol (11). This hydroxyl corresponds to the lone active site, hydrogen-bonding moiety of the first-generation inhibitors and thus is a universal contributor to binding enthalpy. The P1–P1' backbone atoms of nelfinavir, which derives little of its binding affinity from enthalpic interactions (12% at 37 °C), differ from those of JE-2147 and KNI-272 only in the replacement of the Apns P1 carbonyl with a methylene group. Nelfinavir contains a JE-2147-like P2 and a KNI-272-like P2' (Figure 1). Thus, the short hydrogen bond between the P1 carbonyl of JE-2147 and Asp25B represents an attractive source of the observed differential enthalpy. However, replacement of the P1 carbonyl with a methylene, in the context of a related Apns inhibitor, results in no overall loss in potency ( $IC_{50}$  of 18 vs 15 pM) (42). Thus, neither the active site hydrogen bonds, the S2 pocket, nor the S2' pocket appears to account for the differential binding enthalpy of the Apns inhibitors.

Enthalpic binding of JE-2147 and KNI-272 is matched by a reduction in binding entropy as compared to other inhibitors (9, 11). The desolvation entropy gained upon binding is proportional to the buried surface area. JE-2147 and KNI-272 exhibit buried surface areas comparable to that of indinavir, which is 10 kcal more entropically favorable (9, 11). Thus, the JE-2147 complex must have less internal entropy (fewer internal degrees of freedom) than the entropy-driven inhibitor complexes. The high resolution and low  $B$  factors of the current structure support our model of damped vibrational modes in the JE-2147–HIV Pr complex. Globally distributed enthalpic interactions in the JE-

2147–HIV Pr complex may bleed off entropy from the system by reducing the number of conformational states available to the protease–inhibitor complex.

**Dimer Interface Motion and Protease Function.** As noted earlier, the dimer interface of this structure is subject to elevated anisotropic motion in the plane of the interface. Clustering analysis of ADP direction profiles and TLS rigid body analysis of the interface indicate that the interface  $\beta$ -sheets exhibit motion distinct from the rest of the protein. HIV Pr has a nanomolar dimerization constant, which speaks to the strength of the dimer interface interactions in the absence of substrate. Nevertheless, unfolding kinetics of HIV Pr indicate that, when bound to inhibitors, the interface  $\beta$ -sheets unfold prior to the remainder of the dimer (43). Nondenaturing, NMR studies of the protease bound to DMP-323 and P9941 show slow relaxation on the >0.5 ms time scale for dimer interface residues 4–6 and 95–98 (44, 45). These slow time scale relaxations for residues 4–6 are consistent with the bifurcated density seen for Thr4A in the JE-2147–HIV Pr complex. This interface mobility was not seen in the unbound protease, suggesting that substrate binding slackens structural constraints at the interface.

A structural comparison of the apo dimer (PDB entry 3hvp) to that of the JE-2147–HIV Pr complex indicates that JE-2147 binding induces an upward and inward rotation of the monomers. A similar rotation was observed in a study of substrate binding to either HIV or SIV Pr (46). Rotation of the protease upon inhibitor binding is coupled to the creation of a stable association of the enzyme's flaps (44) and a coalescing of the core of the protease around the inhibitor itself. The correlated motion of the active site and the helices of the dimer implied by our ADP clustering and TLS analysis (cluster 2) and the agreement in  $B$  factors of these two regions (Figure 5B) suggest a role of the helices in linking the active site to the dimer interface. Two possibilities present themselves as structural models for the mobility exhibited by the dimer interface of the current structure: dimer interface relaxation provides an entropic compensation for fixing the active site residues and the flaps upon inhibitor binding, and/or the loosening of the dimer interface affords the active site the additional conformational freedom necessary for substrate binding and catalysis.

## CONCLUSION

Adaptation by HIV Pr to current therapeutics is emerging and spreading, with transmission of multi-drug-resistant virus reported (47). JE-2147 is a second-generation inhibitor, with improved potency against HIV Pr and a drug resistance profile different from those of the currently available therapeutics (8). JE-2147 possesses no more hydrogen bonds to the protease than the inhibitors of Figure 1, yet binds with an enthalpic term that is up to 10 kcal more favorable. This enthalpically driven binding of JE-2147 to HIV Pr appears to influence the global motion of the protease, as is evident from the low  $B$  factors of the structure. ADP profile analysis of the JE-2147–HIV Pr complex suggests that JE-2147 binding induces concerted motion in the prime side binding loops of the dimer due to an induced fit, which may promote enthalpic interactions among these loops. Comparison of the thermodynamically characterized inhibitors of Figure 1 indicates that enthalpic inhibitors tend to resemble the natural

substrate specificity of HIV Pr (Phe, Pro, and Leu) in their P1 and P1' moieties, and thus take advantage of the evolved binding conformation of the enzyme. Enthalpic inhibition of the protease has been suggested to allow the design of additional flexibility, and thus entropic loss upon binding, into an inhibitor (9). This flexibility would allow the inhibitor to conform to the altered active site of resistant enzymes. An alternate strategy for inhibitors such as JE-2147 may be to reduce the deleterious effects of resistance mutations by preventing reorganization of the protease upon mutation via distributed enthalpic interactions. Further, enthalpic inhibitors may extend their limit on binding affinity by stabilizing the protease and, thus, reducing inhibitor off rates.

## ACKNOWLEDGMENT

We thank Erin M. O'Donnell, Alison Bahr, and Scott Pegg for their careful reading of the manuscript. We thank Dr. David Matthews and the Agouron Corp. for providing the JE-2147 used for these studies. Some crystallographic data were collected at the Stanford Synchrotron Radiation Laboratory (SSRL) funded by the Department of Energy (BES and BER) and the National Institutes of Health (NCRR and NIGMS).

## SUPPORTING INFORMATION AVAILABLE

Clustered ADP difference profiles for the JE-2147 complex. In the production of the  $\Delta$  matrix using the program ANISOANAL, the variable DURANGE was set to 3.0, which scaled the output so as to include all data points in the resulting matrix. The color scale is from black (little common rigid body motion) to aqua (a common element of rigid body motion). This material is available free of charge via the Internet at <http://pubs.acs.org>.

## REFERENCES

1. UNAIDS and World Health Organization (2000).
2. Kohl, N. E., Emini, E. A., Schleif, W. A., Davis, L. J., Heimbach, J. C., Dixon, R. A., Scolnick, E. M., and Sigal, I. S. (1988) *Proc. Natl. Acad. Sci. U.S.A.* **85**, 4686–4690.
3. McQuade, T. J., Tomasselli, A. G., Liu, L., Karacostas, V., Moss, B., Sawyer, T. K., Heinrikson, R. L., and Tarpley, W. G. (1990) *Science* **247**, 454–456.
4. Wlodawer, A., and Vondrasek, J. (1998) *Annu. Rev. Biophys. Biomol. Struct.* **27**, 249–284.
5. Coffin, J. M. (1995) *Science* **267**, 483–489.
6. Mahalingam, B., Louis, J. M., Hung, J., Harrison, R. W., and Weber, I. T. (2001) *Proteins* **43**, 455–464.
7. Mimoto, T., Kato, R., Takaku, H., Nojima, S., Terashima, K., Misawa, S., Fukazawa, T., Ueno, T., Sato, H., Shintani, M., Kiso, Y., and Hayashi, H. (1999) *J. Med. Chem.* **42**, 1789–1802.
8. Yoshimura, K., Kato, R., Yusa, K., Kavlick, M. F., Maroun, V., Nguyen, A., Mimoto, T., Ueno, T., Shintani, M., Falloon, J., Masur, H., Hayashi, H., Erickson, J., and Mitsuya, H. (1999) *Proc. Natl. Acad. Sci. U.S.A.* **96**, 8675–8680.
9. Velazquez-Campoy, A., Kiso, Y., and Freire, E. (2001) *Arch. Biochem. Biophys.* **390**, 169–175.
10. Boden, D., and Markowitz, M. (1998) *Antimicrob. Agents Chemother.* **42**, 2775–2783.
11. Velazquez-Campoy, A., Luque, I., Todd, M. J., Milutinovich, M., Kiso, Y., and Freire, E. (2000) *Protein Sci.* **9**, 1801–1809.
12. Todd, M. J., Luque, I., Velazquez-Campoy, A., and Freire, E. (2000) *Biochemistry* **39**, 11876–11883.
13. Toth, M. V., and Marshall, G. R. (1990) *Int. J. Pept. Protein Res.* **36**, 544–550.
14. Williams, J. W., and Morrison, J. F. (1979) *Methods Enzymol.* **63**, 437–467.
15. Rozzelle, J. E., Dauber, D. S., Todd, S., Kelley, R., and Craik, C. S. (2000) *J. Biol. Chem.* **275**, 7080–7086.
16. Otwinowski, Z., and Minor, W. (1997) Processing of X-ray Diffraction Data Collected in Oscillation Mode, in *Methods in Enzymology, Volume 276: Macromolecular Crystallography* (Carter, C. W., Jr., and Sweet, R. M., Eds.) Part A, pp 307–326, Academic Press, New York.
17. Baldwin, E. T., Bhat, T. N., Gulnik, S., Liu, B., Topol, I. A., Kiso, Y., Mimoto, T., Mitsuya, H., and Erickson, J. W. (1995) *Structure* **3**, 581–590.
18. Wlodawer, A., Miller, M., Jaskolski, M., Sathyaranayana, B. K., Baldwin, E., Weber, I. T., Selk, L. M., Clawson, L., Schneider, J., and Kent, S. B. (1989) *Science* **245**, 616–621.
19. Navaza, J. (1994) *Acta Crystallogr. A50*, 157–163.
20. Collaborative Computational Project No. 4 (1994) *Acta Crystallogr. A50*, 760–763.
21. Brunger, A. T., Adams, P. D., Clore, G. M., DeLano, W. L., Gros, P., Grosse-Kunstleve, R. W., Jiang, J. S., Kuszewski, J., Nilges, M., Pannu, N. S., Read, R. J., Rice, L. M., Simonson, T., and Warren, G. L. (1998) *Acta Crystallogr. D54*, 905–921.
22. Perrakis, A., Morris, R., and Lamzin, V. S. (1999) *Nat. Struct. Biol.* **6**, 458–463.
23. Muller, K., Amman, H. J., Doran, D. M., Gerber, P. R., Gubernator, K., and Schrepfer, G. (1988) *Bull. Soc. Chim. Belg.* **97**, 655–667.
24. Sheldrick, G. M., and Schneider, T. R. (1997) *Methods Enzymol.* **277**, 319–343.
25. Sobolev, V. S. A., Prilusky, J., Abola, E. E., and Edelman, M. (1999) *Bioinformatics* **15**, 327–332.
26. Kleywegt, G. J., and Jones, T. A. (1994) *ESF/CCP4 Newsletter* **31**, 9–14.
27. Skarzynski, T., and Leslie, A. (1998) Imperial College, London.
28. Schomaker, V., and Trueblood, K. N. (1998) *Acta Crystallogr. B54*, 507–514.
29. Howlin, B., Butler, S. A., Moss, D. S., Harris, G. W., and Driessens, H. P. C. (1993) *J. Appl. Crystallogr.* **26**, 622–624.
30. Eisen, M. B., Spellman, P. T., Brown, P. O., and Botstein, D. (1998) *Proc. Natl. Acad. Sci. U.S.A.* **95**, 14863–14868.
31. Merritt, E. A. (1999) *Acta Crystallogr. D55*, 1109–1117.
32. Wang, Y. X., Freedberg, D. I., Yamazaki, T., Wingfield, P. T., Stahl, S. J., Kaufman, J. D., Kiso, Y., and Torchia, D. A. (1996) *Biochemistry* **35**, 9945–9950.
33. Kageyama, S., Mimoto, T., Murakawa, Y., Nomizu, M., Ford, H., Jr., Shirasaka, T., Gulnik, S., Erickson, J., Takada, K., Hayashi, H., et al. (1993) *Antimicrob. Agents Chemother.* **37**, 810–817.
34. Mimoto, T., and Kiso, Y. (1992) *Chem. Pharm. Bull.* **40**, 2251–2253.
35. Rosenfield, R. E., Trueblood, K. N., and Dunitz, J. D. (1978) *Acta Crystallogr. A34*, 828–829.
36. Rose, R. B., Craik, C. S., Douglas, N. L., and Stroud, R. M. (1996) *Biochemistry* **35**, 12933–12944.
37. Kantor, R., Machekano, R., Gonzales, M. J., Dupnik, K., Schapiro, J. M., and Shafer, R. W. (2001) *Nucleic Acids Res.* **29**, 296–299.
38. Scott, W. R., and Schiffer, C. A. (2000) *Struct. Folding Des.* **8**, 1259–1265.
39. Tozser, J., Yin, F. H., Cheng, Y. S., Bagossi, P., Weber, I. T., Harrison, R. W., and Oroszlan, S. (1997) *Eur. J. Biochem.* **244**, 235–241.
40. Wu, J., Adomat, J. M., Ridky, T. W., Louis, J. M., Leis, J., Harrison, R. W., and Weber, I. T. (1998) *Biochemistry* **37**, 4518–4526.
41. Martin, J. L., Begun, J., Schindeler, A., Wickramasinghe, W. A., Alewood, D., Alewood, P. F., Bergman, D. A., Brinkworth, R. I., Abbenante, G., March, D. R., Reid, R. C., and Fairlie, D. P. (1999) *Biochemistry* **38**, 7978–7988.
42. Le, V., Mak, C. C., Lin, Y., Elder, J. H., and Wong, C. (2001) *Bioorg. Med. Chem.* **9**, 1185–1195.

43. Panchal, S. C., and Hosur, R. V. (2000) *Biochem. Biophys. Res. Commun.* 269, 387–392.
44. Ishima, R., Freedberg, D. I., Wang, Y. X., Louis, J. M., and Torchia, D. A. (1999) *Struct. Folding Des.* 7, 1047–1055.
45. Nicholson, L. K., Yamazaki, T., Torchia, D. A., Grzesiek, S., Bax, A., Stahl, S. J., Kaufman, J. D., Wingfield, P. T., Lam, P. Y., Jadhav, P. K., et al. (1995) *Nat. Struct. Biol.* 2, 274–280.
46. Rose, R. B., Craik, C. S., and Stroud, R. M. (1998) *Biochemistry* 37, 2607–2621.
47. Hecht, F. M., Grant, R. M., Petropoulos, C. J., Dillon, B., Chesney, M. A., Tian, H., Hellmann, N. S., Bandrapalli, N. I., Digilio, L., Branson, B., and Kahn, J. O. (1998) *N. Engl. J. Med.* 339, 307–311.
48. McRee, D. E. (1999) *J. Struct. Biol.* 125, 156–165.
49. Kaplan, W., and Littlejohn, T. G. (2001) *Briefings Bioinf.* 2, 195–197.
50. Wallace, A. C., Laskowski, R. A., and Thornton, J. M. (1995) *Protein Eng.* 8, 127–134.

BI011781Z